scientific reports



OPEN

Process and property assessment of liquid metal spray deposition towards scalable and reliable stretchable electronics

Maximilian Krack^{1,2}, Rathul Nengminza Sangma³, Lennert Purnal^{1,2}, Parth Vinayakrao Sewlikar⁴, Dieter Reenars^{1,2}, Fatemeh Sahraeeazartamar⁴, Joost Brancart⁴, Guy Van Assche⁴, Iris De Graeve⁴, Tom Hauffman⁴, Michaël Daenen^{1,2}, Seppe Terryn^{3,4}, Bram Vanderborght³, Monika Rai^{1,2} & Wim Deferme^{1,2⊠}

Liquid metal stretchable electronics combine exceptional softness, stretchability, and self-healing capabilities, making them ideal for smart wearables and soft robotics. A key fabrication approach involves pneumatic spray deposition into patterned structures. However, the impact of process parameters on LM deposition remains poorly understood, largely due to reliance on manual airbrushing-limiting both scalability and reliability. This work addresses these challenges with a custom-built automated spray coater, offering precise control over key parameters such as flow rate, pressure, and spray distance. Through systematic process—property analysis, we reveal that rougher coatings improve device yield (approaching 100%) but compromise long-term reliability. Finer linewidths (0.25 mm) fail earlier in cyclic testing and exhibit reduced self-healing compared to wider lines (≥ 0.5 mm). Scalability is demonstrated through the fabrication of a large-area wearable strain sensor (70 \times 150 mm) for human motion capture. These findings offer critical insights into process—structure—property relationships, paving the way for reliable, scalable LM-based stretchable electronics.

Keywords Liquid metal, Stretchable electronics, Spray deposition, Strain sensor, Reliability

Conventional electronics, while reliable and high-performing, are often brittle and inelastic, making them unsuitable for a wide range of emerging applications. As the demand for soft and wearable devices grows, especially in the health, consumer and soft robotics sector, there is a need for electronics that can conform to the human body and mimic the flexibility of living organisms^{1–3}. Recent advancements in flexible electronics have expanded to include soft, stretchable electronics capable of withstanding strains of several hundred percent^{4–6}. Stretchable electronics offer several key advantages. Their intrinsic softness not only protects them from damage but also safeguards the environment they interact with. As a result, they are ideal for delicate tasks, such as soft sensors in grippers designed to handle fragile fruits or vegetables^{7–9}, or smart soft devices that interact safely with humans¹⁰.

To achieve this level of softness, traditional rigid interconnections are replaced with stretchable conductors that maintain conductivity under strain such as polymer composites, spring-like metallic structures and gallium-based liquid metals (LM) $^{11-17}$. *Galinstan* (Ga–In–Sn alloy), stands out for its high electrical conductivity (3.46 \times 10^6 S/m), low melting point (11°), low vapour pressure ($<10^{-6}$ Pa at 500° C), and minimal hysteresis, making it well-suited for soft electronics 11 . To enable stretchability in liquid metal-based stretchable electronics (LMSE), Galinstan is typically deposited onto stretchable elastomeric substrates and encapsulated within the same material, allowing seamless conformability 18 . Gallium's thin native oxide layer (3–5 nm) allows the Galinstan to form non-spherical shapes and enabling versatile patterning 19,20 . Elastomers like Smooth-On silicones, such as Ecoflex, are widely used due to their excellent mechanical properties, biocompatibility, and affordability $^{21-23}$.

¹Institute for Materials Research, Hasselt University, Hasselt 3500, Belgium. ²IMEC vzw, Division IMOMEC, Diepenbeek 3590, Belgium. ³Brubotics, Vrije Universiteit Brussel and IMEC, Elsene 1050, Belgium. ⁴Materials and Chemistry and Sustainable Materials Engineering, Vrije Universiteit Brussel, Elsene 1050, Belgium. email: wim.deferme@uhasselt.be

Various methods for depositing LM onto stretchable substrates have been explored, such as direct writing, filling, inkjet and spray deposition^{24–32}. A quantitative comparison between techniques is provided in Table S1 (Supplementary Information). Spray coating, based on pneumatic atomization (a technique that uses pressurized gas to break a liquid stream into fine droplets) is a promising method for patterning LMs onto stretchable substrates. Combined with stencil-based patterning, it enables scalable, high-throughput deposition on diverse surfaces with minimal setup and roll-to-roll compatibility^{31,32}. Zhang et al. first demonstrated the atomized spraying of LM and its capability to deposit on nearly any substrate type³³. Since then, few studies have advanced LM spray deposition to improve LMSE printability and performance. However, most current approaches rely on manual airbrushing, which lacks precision and automation, limiting control over spray parameters and reproducibility^{34–37}. This presents key challenges in achieving uniform LM coatings, understanding LM-stencil interactions, and ensuring consistent device performance. Non-uniform deposition can lead to circuit failures, localized heating, and signal instability under strain^{38,39}. Addressing these limitations is essential for achieving reliable, scalable fabrication^{24,40}.

To overcome limitations in LMSE fabrication, this work presents a detailed assessment of spray parameters affecting LM coating quality and device performance. An affordable, automated spray coater (ASC) has been developed using a modified 3D printer with precise control over nozzle speed, flow rate, height, and pressure. Spray behavior is characterized via laser fan imaging⁴¹. A full factorial analysis is employed to systematically optimize spray parameters based on key performance metrics i.e. electrical resistance, surface topography, and line resolution. Reliability is validated through cyclic strain testing of LM interconnects, demonstrating stable operation under strains up to 75%. To highlight the scalability and real-world applicability of the process, a wearable strain sensor is fabricated and thoroughly characterized. Finally, a summary table outlines optimal parameter combinations, serving as a practical reference for researchers and industry affiliates aiming to adopt or adapt this fabrication approach.

Results

Automated spray deposition of LM

In this section, the properties and capabilities of the ASC are introduced. The schematic of the ASC system (actual image and video as in Fig. S1/Video S1 Supplementary Information) in Fig. 1a consists of the following four key components:

- A commercially available 3D printer is responsible for all motion control. Homogeneous printing area 30 by $30~{\rm cm}^2$.
- A regulatory pressure valve that can be connected to any gas source. Nitrogen and air are used in this work for pneumatic atomization.
- · A custom-made syringe pump powered by an Arduino, necessary to ensure a constant supply of LM.
- A custom-designed 3D printed spray nozzle with both air and LM inlets (Fig. S2, Supplementary Information).

These low-cost, readily available, and reproducible components are key to scalable, cost-effective implementation. The optimized LMSE fabrication process is shown in Fig. 1b. The humidity is in a range between 36% and 44% as it was reported that humidity influences the adhesion of LM onto silicone substrates⁴². The temperature is room-temperature. The process begins with adhering electronic components, with electrodes facing down, in predefined spots on an acrylic baseplate (1). An adhesion-enhancing primer is then sprayed onto the components to improve adhesion to the silicone substrate. Ecoflex 00-30 is chosen as the stretchable encapsulation for all LMSEs in this work due to its excellent mechanical properties and processability. Its low viscosity and long pot-life of 40 min provide ample time for vacuum degassing, which is essential for eliminating air pockets that could lead to premature device failure⁴³. Ecoflex is injected into the molds (2), with the silicone pushed into a syringe by a lever device to prevent air trapping. Injection molding is crucial for batch fabrication, as it ensures multiple devices can be produced in a single batch while maintaining flatness across the batch. This is important for stencil printing, as the stencil must make an even contact with each device to prevent underspraying (Fig. S3, Supplementary Information). Before applying the stencil, the device is flipped to expose the electrodes of the PCB (3). After the stencil is applied, LM is sprayed over the stencil (4) with the ASC, and the stencil is carefully removed. The devices are then encapsulated with Ecoflex (5). Blade coating is chosen as the method of encapsulation. It is a faster process and ensures minimum LM displacement. Finally, the LMSE is released from the mold (6). All devices in this paper are fabricated using an iteration of this process.

The controllability and quality of the LM spray with the custom nozzle are highlighted in Fig. 1c. For the spray imaging, a green laser, nozzle, and dark background (Fig. S4, Supplementary Information). The nitrogen pressure is slowly changed from 0 to 5 bar, then back to 0 bar, at a constant flow rate of 1.6 ml/min. Initially, droplets are generated at the orifice, but no atomization occurs (liquid breakdown into smaller droplets), which leads to a dripping behavior. This behavior persists until a critical pressure of 0.9 bar is reached, at which point the droplets burst explosively. This leads to a fully developed spray sufficient for deposition. Galinstan exhibits exceptionally high surface tension (535–718 mN/m), making controlled atomization particularly challenging⁴⁴. The initial droplets, therefore, require significant pressure for atomization. As the pressure increases slowly to 5 bar, the spray becomes denser and more jet-like, with a clearer Gaussian distribution of droplets. This is reflected in the spray intensity distribution (Fig. S5, Supplementary Information). A similar trend is followed when the pressure is slowly decreased from 5 bar to 0 bar. Below 1 bar, the spray enters a weak regime with larger, less uniform droplets⁴¹. At 0 bar, the LM exits as a continuous stream approximately that of the nozzle diameter, retaining its shape due to inertia before breaking into individual droplets from the Plateau–Rayleigh instability⁴⁵.

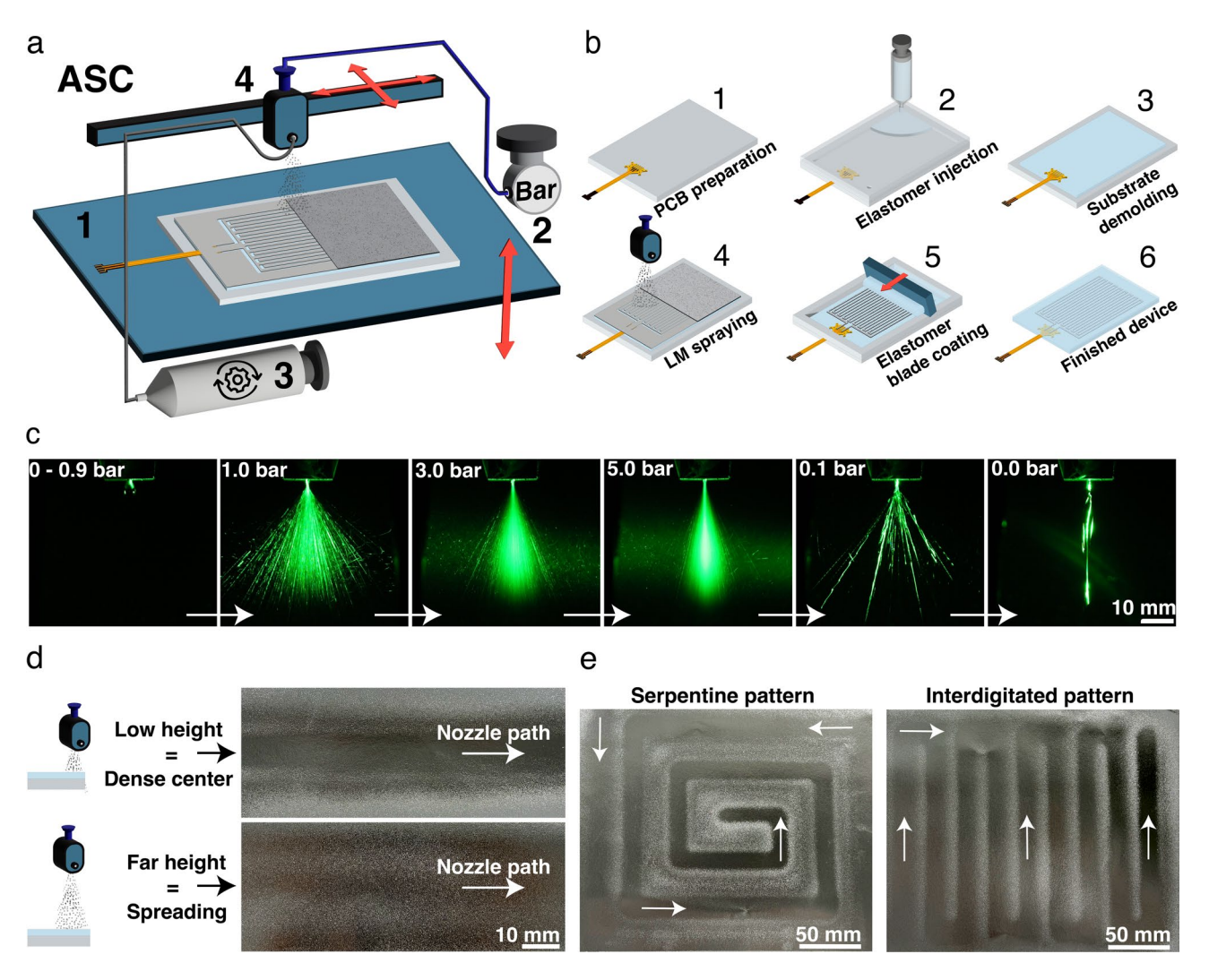


Fig. 1. (a) Schematic of the automated spray coater (ASC) with a 3D printed nozzle, automated syringe pump and pressure valve, (b) LMSE fabrication steps: (1) PCB placement, (2) Injection molding Ecoflex substrate, (3) Substrate release and flip, stencil application, (4) LM spray via ASC and stencil lift-off, (5) Silicone encapsulation by blade coating, (6) Device release, (c) Spray nozzle undergoing a pressure sweep from 0→5→0 bar at a constant flow rate of 1.6 ml/min, (d) Spray patterns with varying nozzle-to-substrate height: top—100 mm with dense center and bottom—250 mm with large spread, (e) A serpentine and an interdigitated pattern deposited at 100 mm spraying height demonstrate the controllability of the ASC.

The spray path (trajectory and pattern of the liquid) of the system demonstrates excellent controllability in its direction. With the controllable spray, uniform and consistent patterns can be deposited through reproducible spray paths as shown in Fig. 1d. Adjusting the height affects the spread of the LM, where close heights result in patterns with dense centers and printing at far heights results in more spreading. The system is also capable of printing precise uniform patterns with set line spacing, demonstrated with serpentine and interdigitated patterns as shown in Fig. 1e. This precise control over the spray path lays the foundation of depositing uniform coatings, which is discussed in the following section.

Investigation of liquid metal coatings

After establishing the uniform and reproducible spray method, sprayed LM coatings are analyzed to uncover key insights into their formation and behavior. This knowledge informs the following sections, which explore the mechanics of LMSE scalability, patterning, and reliability. The spray system is first characterized and optimized, identifying ideal operating ranges: low flow rates of 0.7 ml/min (LFR) and high flow rates of 1.6 ml/min (HFR), and low pressures of 2 bar (LP) and 5 bar (HP). The initial optimization of the ASC process is a series of one-factor-at-a-time (OFAT) experiments and an L3 P3 Taguchi orthogonal array (Figs. S6–S9, Table S2, Supplementary Information)⁴⁶.

Oxide layer formation

Scanning electron microscopy (SEM) images attached along with their respective energy dispersive X-ray spectroscopy (EDX) distributions of LM coatings are shown in Fig. 2a. The coatings are sprayed from a height of 100 mm onto a glass substrate at LP and HP. It is unclear if spray deposition increases oxide content^{33,34,36}. It has been known that finer droplets possess a higher surface-to-volume ratio, hypothetically leading to more oxide build-up in the coating. Higher pressure may cause droplet intermixing that repeatedly reforms the oxide layer. EDX showed no compositional differences between LP and HP coatings, despite topological changes. To confirm that nitrogen is not suppressing oxide formation, LM coatings are also sprayed using air (Fig. S10). Similar results show no oxide build-up, likely because the native oxide layer is only a few nanometers thick and droplets lack sufficient flight time to form a full oxide skin. Additionally, with the nozzle moving at a speed of 25 mm/s, there may not have been enough time for LM turbulence and intermixing.

Surface topography

Typical surface mapping of LM coatings deposited onto both soft Ecoflex polymer and hard glass substrates at LP and HP as well as LFR and HFR are shown in 2b. The images are captured using laser confocal microscopy

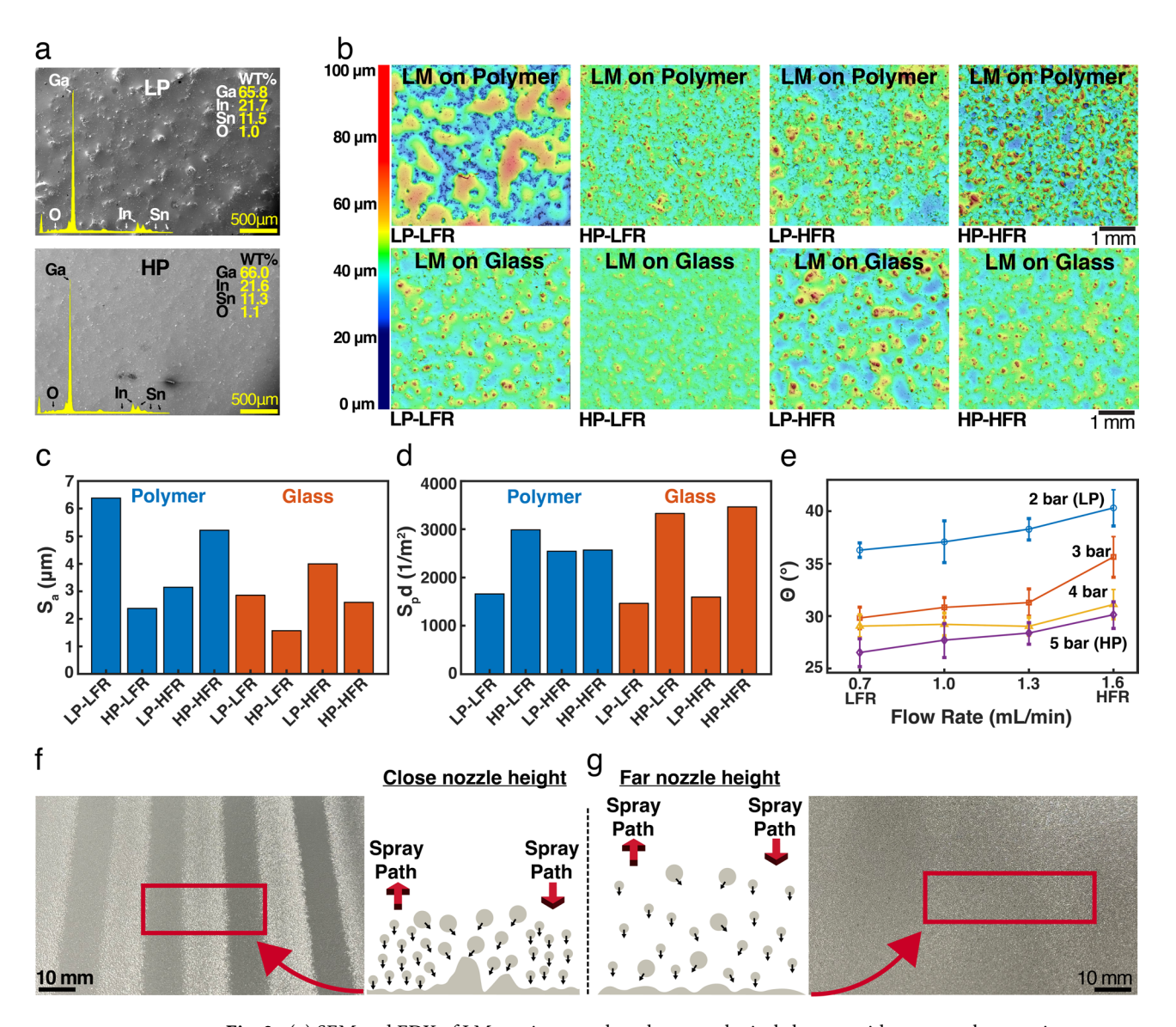


Fig. 2. (a) SEM and EDX of LM coatings on glass show topological changes with pressure, but consistent composition, indicating minimal material impact, (b) LSM images reveal substrate and parameter dependent coating differences on polymer and glass, (c,d) Surface roughness and peak density variation: polymer shows high roughness at LP-LFR due to delamination and at HFR due to coalescence; glass shows reduced roughness at HP from LM spreading. Peak density increases on glass at HP due to finer atomization, (e) Spray angles decrease with HP (stronger aerodynamic forces) and increase with HFR (greater LM volume), (f,g) Coating formation on glass is modeled from spray angles at 100 mm and 250 mm heights; uniform coverage is achieved at 250 mm with 62–68% path overlap.

(LSM), and their respective quantitative surface properties are measured and shown in Fig. 2c and d. The surface properties of LM differ significantly between soft and hard substrates, driven by how high kinetic energy droplets interact upon impact. On soft, viscoelastic polymers, some of the droplets' kinetic energy is absorbed. This means that the LM droplets do not spread into a film but instead accumulate into larger droplets, which is evident when comparing the HP images of polymer and glass. In contrast, on glass, which does not absorb kinetic energy on impact, the droplets dissipate energy by spreading into a film. This energy consideration provides an additional challenge in creating high-quality LMSE.

- Roughness Surface area roughness (S_a) is quantified in Fig. 2c. On glass, S_a decreases at HP due to the droplets spreading from high impact forces but increases at HFR as droplets become larger⁴⁷. On polymer substrates, an unusual interaction occurs at LP-LFR, resulting in the LM delaminating into large, connected islands, leading to high S_a values. The delamination is further apparent from surface skewness measurements (Fig. S11, Supplementary Information). It is most likely a combination of insufficient spreading (and adhesion) of the droplets and the high surface tension of LM. At HP-LFR, this behavior disappears, as smaller droplets atomized by higher pressure are less likely to merge into large islands because of their lower volume and oxide skin. They also possess higher kinetic energy at HP, resulting in more spreading even on the soft surface.
- Peak density Fig. 2d shows the number of individual peaks in a given area. On the glass substrate, the peak density follows a reverse trend compared to the previous graph. Although the peaks decrease in height, as depicted in the S_a values, the overall density of peaks sharply increases at high pressure. This is due to the generation of a larger number of smaller droplets during atomization at high pressure, which remain as separated peaks on the substrate. On the polymer substrate, the peak density is initially lower at LP-LFR because the droplets coalesce into islands as previously described. At HFR, droplets coalesce, reducing peak density. This results in larger individual droplets. The peak density, therefore, stays the same while roughness sharply increases, as previously explained.

From a coverage aspect, LP-LFR on polymer should not be used to avoid delamination, which can lead to non-uniform LMSE. However, the impact of topological properties on LMSE performance is further investigated in the following sections.

Large area coating

To enable the deposition of uniform, large area coatings that exceed the width of a single spray path, the (simplified) coverage radius of the spray for any given height must be known. With a known radius, the line spacing between multiple spray paths and, therefore, the overlapping percentage can be calculated precisely. The spray angle, which is the angle between nozzle orifice and spray, is measured for different flow rates and pressure values using 20 images per parameter combination with the setup described previously (Fig. 1b) and analyzed with Image] software. The spray takes 2–5 s to fully develop, with shorter times observed at higher flow rates (Fig. S12, Supplementary Information). Figure 2e presents the spray angles for various conditions, revealing that the spray angle increases with flow rate and decreases with pressure. At higher pressures, aerodynamic forces become more significant, streamlining the flow and narrowing the spray angle. The higher momentum of the liquid jet at increased pressures helps to maintain a focused stream, reducing the spray angle. Conversely, a higher flow rate increases the volume of ejected LM, broadening the spray angle⁴⁸. By assuming the spray shape to be an ideal cone, the coverage radius r(mm) can be derived using Eq. (1).:

$$r = d \times tan\frac{\theta}{2},\tag{1}$$

where d is the nozzle to substrate height and θ (rad) is the spray angle. Other important merits, such as coverage area and LM consumption, can also be derived from the spray angle (Eqs. S1 and S2, Supplementary Information).

The overlapping of several spray paths of a single nozzle at different nozzle heights to deposit large-area coatings, which can be scaled infinitely, is illustrated in Fig. 2f and g. The overlapping percentage of the spray paths is calculated from the previous section. The results show that due to the unique properties of LM, achieving a uniform large coating can be challenging. The velocity and droplet size distribution across the spray path are not uniform, as previously mentioned. Overlapping the sprays at a close height of 100 mm with a 50% overlap causes larger, slower droplets to accumulate into a thick and rough layer due to unwanted coalescence between spray paths, as seen in Fig. 2f. This effect is further exacerbated by LM's high surface tension and poor wetting on non-metallic surfaces. In contrast, directly below the nozzle, the LM forms a smoother layer due to the higher pressure. To achieve uniform coatings, the strategy involves evening out the distribution of droplet size and velocity by significantly increasing the height to the substrate. The mechanism is shown in the right-hand schematic. In Fig. 2g, the height is increased to 250 mm. Overlapping spray paths between 62% and 68%, based on prior spray angle calculations, results in a uniform coating with thickness deviations of only 5% (Fig. S13, Supplementary Information). However, the roughness seems higher compared to low-height coatings, which exhibit a flat, more reflective appearance. In conclusion, to deposit large-area uniform coatings, the nozzle height to substrate should be increased to allow the spray to develop and avoid unwanted coalescence.

Analyzing LMSE processing with ASC

Stencil printing with spray deposition remains the most common method for patterning LM in the literature²⁴. However, due to the lack of controllability in conventionally used airbrushes, studying LM stencil printing has been challenging^{34,36}. In this section, the effects of spray parameters and the coating properties, which were

previously discussed, are investigated to understand their influence on the properties of stencil-printed LMSE. These include the overall yield of LMSE, as well as topographical, electrical, and geometrical properties. This is enabled with a full factorial analysis between flow rates of 0.7 ml/min and 1.6 ml/min (LFR-HFR) and pressures between 2 bar and 5 bar (LP-HP), including intermediate values.

Design of the LMSE

A standardized LMSE is designed and employed throughout the full factorial analysis. For accurate electrical characterization, a one-wire LMSE compatible with 4-wire measurements, as seen in Fig. 3a, is designed. Reliable electrical interconnection and measurements are enabled with a patented flex PCB from our research group⁴⁹. The flex PCBs differ from traditional interconnection methods, such as rigid wires, which can move around and displace the LM or tear the encapsulation⁵⁰. The encapsulation is designed as a dogbone which ensures proper tensile testing⁵¹. For application purposes, four different linewidths, which all lie on the same stencil, are investigated: 1 mm, 0.5 mm, 0.25 mm, and 0.1 mm. Thanks to the scalability and controllability of the ASC, it is possible to fabricate 8 samples within a single batch at a nozzle height of 100 mm.

Influence on LMSE yield

The yield of the functioning LMSE during the full factorial analysis is investigated and further characterized. A fully functioning LMSE is defined as one in which the LM connection is uninterrupted, enabling electrical measurements between the two flex PCBs. The main failure mode observed during the full factorial analysis is LM lift-off by the stencil (Fig. S14, Supplementary Information). Ideally, stencil lifting should not affect LM,

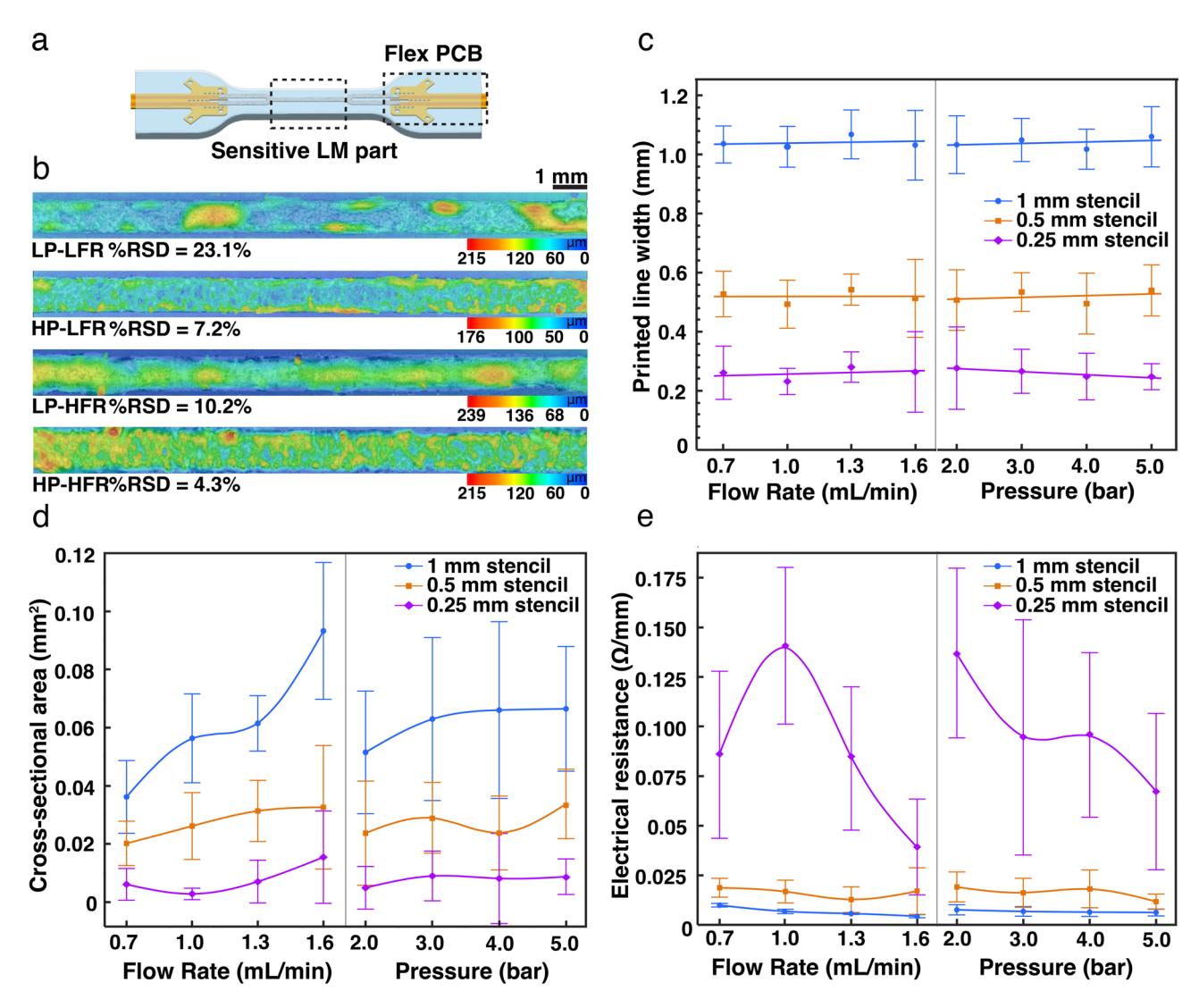


Fig. 3. (a) Dogbone test device with 4-wire measurement focuses on the central LMSE region, excluding wire/contact resistance, (b) Contour images of LM wires at varying flow rates show best uniformity at HP-HFR, due to enhanced coverage, atomization, and reduced LM lift-off, (c-e) LM properties printed with 1, 0.5, and 0.25 mm stencils across flow rate and pressure in a full factorial setup (details in Fig. S19). Each data point reflects combinations of spray parameters; mean values and error bars are based on 16 samples.

but cohesive pathways extend onto the stencil. Lifting the stencil can not only degrade the line-edge roughness but also cause complete lift-off if the cohesion of the LM exceeds its adhesion to the substrate. The best results, therefore, are achieved with rough coatings. These possess more pronounced hills and valleys, providing high-stress points for the surface oxide, which can break more easily when shearing the stencil off the substrate⁵². The coatings deposited at LP are more likely to delaminate as the droplets form smoother cohesive pathways with fewer breakage points. This issue is amplified by the width of the stencil opening: the smaller the opening, the weaker the adhesion to the substrate, and the more likely the LM is to lift off. Patterns down to 0.1 mm can be fabricated (Fig. S15, Supplementary Information), but yields are inconsistent (50%), so they were excluded. This is generally due to the stencil lifting off the LM from the substrate. Different stencils are needed to achieve these finer resolutions, which would, in turn, trade-off scalability due to extensive stencil preparations³¹. Additionally, adhesion of the LM to the substrate could be improved by altering the surface chemistry of the polymer⁵³. For all widths equal and greater than 0.25 mm, a yield of 100% is achieved at HP-HFR. The worst yield is observed at LP, where the yield is < 50% for 0.25 mm wide LMSE and 90% for 0.5 mm and 1 mm LMSE.

Influence on LMSE topography

The topographical properties of 1 mm wires are shown in Fig. 3b and mostly reflect the properties of the deposited coatings shown in Fig. 2. The LMSE is measured by digital microscopy across the full length of the 20 mm sensitive area. Linewidth was largely independent of spray parameters. The uniformity in thickness of the samples is investigated through their relative standard deviation (RSD), calculated from three different areas of the LM wires. Low RSD values are significant for preventing thin thermal bottlenecks (parts of unusually low cross-sectional area), which can impair the device's reliability under load³⁸. The RSD is heavily influenced by the spray parameters, with the worst values observed at LP-LFR and the best values at HP-HFR for 1 mm wires, which can be attributed to improved coverage and atomization (Fig. S16, Supplementary Information). In HP scenarios, less lifting and pushing occur due to higher peak densities and roughness levels as explained previously. However, the RSD can also be affected by stencil lift-off, where LM can be pushed toward the shearing direction of the stencil or lifted off, as previously elaborated. This is a major reason that affects uniformity in lower-width samples (Fig. S17, Supplementary Information).

Influence on LMSE geometry

The actual printed linewidths, which overall remain constant because they are bound and defined by the dimensions of the stencil, are shown in Fig. 3c. The RSD increases substantially at lower stencil dimensions due to the stencil's resolution (Fig. S18, Supplementary Information). Spray parameters influence RSD. The lowest RSD values for 1 mm wires are observed in LMSE with HP-LFR with < 5%, while the highest RSD occurs at LP-HFRs, around 7%. At HFR, coatings are thicker, which can lead to LM lifting due to cohesion (at LP), as well as outward flow when the hydrostatic pressure inside the printed wire is too high. This adds width to the printed structure. At HP, the additional roughness stabilizes against both outward flow and lift-off as mentioned in section b. For narrower patterns, increasing the flow rate results in a lower RSD until a critical flow rate of HFR, as the hydrostatic pressure is comparatively lower due to the smaller cross-sectional area. The overall cross-sectional area is heavily influenced by spray parameters, as seen Fig. 3d. The cross-sectional area increases with flow rate due to the availability of more LM. This is also true when pressure is increased due to the reduced spray angle as explained in the previous section. As explained previously, narrower patterns are more likely to be affected by LM lift-off especially at higher flow rates, which makes the stencil printing more unpredictable. This explains the reverse trend and larger error bars with 0.5 mm wires deposited at HFR. An interesting interaction is revealed by the full factorial analysis where 0.25 mm patterns deposited at LFR result in a cross-sectional area at a similar level as for 1.3 ml/min. LFR results in overall thinner coatings which is beneficial for narrow 0.25 mm patterns as LM displacement is less likely. This can lead to overall thicker patterns after lifting the stencil.

In conclusion, LM geometry can be negatively impacted by its fluidity, especially during stencil lift-off. While lifting and displacement cannot be fully eliminated, they can be minimized by using higher pressure and avoiding excessive flow rates, highlighting the importance of precise spray parameter control in LM deposition.

Influence on LMSE electrical properties

Resistance per length (Ω /mm) over the deposition parameters is shown in Fig. 3e. As expected and in accordance with the cross-sectional area trend, resistance decreases at higher flow rate and pressure. However, a significant difference between the 0.25 mm wires and the others is evident. Due to excessive LM lifting at 0.25 mm and the lower cross-sectional areas, these devices are more prone to bottlenecks, which negatively impact reproducibility, and sharply increase the bulk resistance³⁹. Resistance decreases at HP/HFR as rougher coatings improve reliability. In this regime, LMSE become much more reproducible, with standard deviations being lower than 5% for 0.5 mm and 1 mm patterns. With electrical resistance and cross-sectional area, the electrical conductivity of the LMSE is estimated. Because the LM is spray-coated, the wires are not perfectly cylindrical or rectangular, as seen in Fig. 3b. Therefore, to estimate the electrical conductivity, the average measured cross-sectional area A is used. Combined with the electrical resistance R, the conductivity σ of the wires, with a length l of 20 mm, can be calculated using Eq. (2):

$$\sigma(S/m) = \rho \times \frac{l \times R}{A}.$$
 (2)

The average conductivity calculated across all parameters ranged between 2.57 and 2.78×10^6 S/m, which is consistent with the literature, though reported values vary⁵⁴. A clear relationship between spray parameters and conductivity is yet again not observed (Fig. S20, Supplementary Information). This further validates that

the LM's composition remains unchanged at different spray parameters as previously described in Fig. 2a. To confirm these results, the conductivity of pristine Galinstan is measured (Fig. S21, Supplementary Information). The average value found is 3×10^6 S/m with differences from the sprayed LM falling within the error margin.

These results demonstrate that the deposited LM properties can be tightly controlled and tuned with the ASC. This makes the ASC suitable for various applications, though the influence of LM properties on other factors, such as reliability, should still be addressed. Further, the stencil remains the biggest uncontrollable variable within the otherwise very controllable process. An effort should be made in future work to automate and optimize the stencil (design and lifting).

Reliability of LMSE

The core functionality of stretchable electronics lies in retaining full functionality during stretching. For real-life application potential, LMSE must maintain their functionality over thousands of stretch cycles. LM has been established as a self-healing conductor that rarely fails on its own⁵⁵. However, the reliability of the full LMSE system depends heavily on the entire assembly: LM, stretchable encapsulation, electrical interconnection, and other rigid components. Devices with 1 mm and 0.25 mm linewidth fabricated at a combination of HP, LP, LFR, and HFR are cycled up to 100,000 times with our in-house cycle testers (Video S2, Supplementary Information). The strain is alternated between 0 and 75%, which is considerably higher than what has been reported in recent literature ^{39,56,57}. This induces fatigue for accelerated life testing. Temperature and humidity are monitored at all times, with average values of $22.2 \pm 0.42^{\circ}$ C and 49.6 ± 6 %, respectively. The three common failure modes discovered in this work are displayed in Fig. 4a as follows:

- Adhesion Loss and Short-Circuiting: During cyclic testing, flex PCBs may detach from silicone, allowing LM
 to flow and cause short circuits. A thin silicone barrier and adhesion primer improve separation and bonding.
- Oxidation and Performance Degradation: Silicone's poor barrier properties allow gradual LM oxidation, reducing conductivity and flexibility. Polymer blends with better oxygen and moisture resistance can slow this process⁵⁸.
- Connector Failure: LM may disconnect from flex PCBs due to the rigid-soft interface. Literature suggests using a stiff mesh around connectors to enhance strain relief and maintain contact⁵⁹.

Oxidation strongly influences LMSE electrical response.

The change in electrical resistance of LMSEs printed with different spray parameters and linewidths (1 mm and 0.25 mm, respectively) after 100,000 cycles is shown in Fig. 4b and c. All samples exhibit an increasing trend in $\Delta R/R_0$, which is related to increased LM oxidation caused by the straining. For rigid electronics, the point of failure typically occurs when rigid wires exhibit a $\Delta R/R_0$ of 20%60, which is reached around 30,000 cycles for most samples. This kind of failure definition has yet to be established for LMSE. Both graphs show that the change in resistance is higher in the relaxed state than in the stretched state. This suggests that material-induced hysteresis occurs when the sample relaxes, caused by changes in the cross-sectional area of the channels through the Poisson effect⁵.

In Fig. 4b, the drop in $\Delta R/R_0$ for the LP-HFR LMSE after 10000 cycles suggests that this parameter combination leads to noisy samples. As discussed previously, LP-HFR more often leads to non-uniform LMSE in terms of their geometry and overall bulkier patterns with moderate roughness (for 1 mm patterns). This can result in conditions where the LM flows more freely upon stretching, which can influence the geometry in a way that positively affects $\Delta R/R_0$ (by offsetting bottlenecks for example). The highest $\Delta R/R_0$ is observed with the HP-HFR and LP-HFR LMSE, and the lowest with the LP-LFR LMSE. The HP-LFR LMSE failed at around 30,000 cycles, but the rate of $\Delta R/R_0$ is just slightly higher than that of LP-LFR. This suggests that $\Delta R/R_0$ is dependent on the roughness of the LM. As previously discussed, the roughness increases from low to high (taking peak density into account) from LP-LFR \rightarrow HP-LFR \rightarrow HP-HFR. LP-LFR LMSE consist of smooth and large peaks, and HP-HFR possess a very rough topography. This enables the following key explanations:

- Rough LM has more stress points, accelerating oxidation during cycling. This rate seems to grow exponentially over cycles when more oxide is introduced as the rate of $\Delta R/R_0$ increases drastically for the rougher HFR LMSE after 20,000 cycles.
- Oxidation has a larger effect on rough patterns and therefore $\Delta R/R_0$, as they possess more pronounced valleys where the LM is very thin. Oxidation of thin areas may lead to bottlenecking or even a full breakage of the LM circuit, which likely caused failure in the HP-LFR sample. Though HP-LFR retained its conductivity back at 0% due to the self-healing capabilities of LM, it ultimately failed after 32,000 cycles, as indicated by the purple arrows.
- Early $\Delta R/R_0$ seems to be driven by the cross-sectional area rather than the roughness as the thinner LMSE are more affected by oxidation (Fig. S22, Supplementary Information). However, once bottlenecking occurs $\Delta R/R_0$ of the rough LMSE increases exponentially, where $\Delta R/R_0$ of the smooth LMSE remains quite linear.

These explanations are validated by what can be extracted from Fig. 4c for cycled 0.25 mm LMSE. A very similar trend of $\Delta R/R_0$ can be seen, only that the absolute values are much higher since the LMSE possess a much lower cross-sectional area by their width. Further, all samples failed before reaching 100,000 cycles, and the same trend can be seen again. The thin and rough HP-LFR LMSE fails first, followed by the roughest HP-HFR sample, which has the highest $\Delta R/R_0$, then the LP-HFR LMSE, and finally the smooth LP-LFR LMSE. Additionally, the self-healing capabilities of the LM are strongly impaired, as most samples failed at 0% and 75% strain simultaneously. This means long-term reliability is both dependent on geometry and topography, where best results are expected

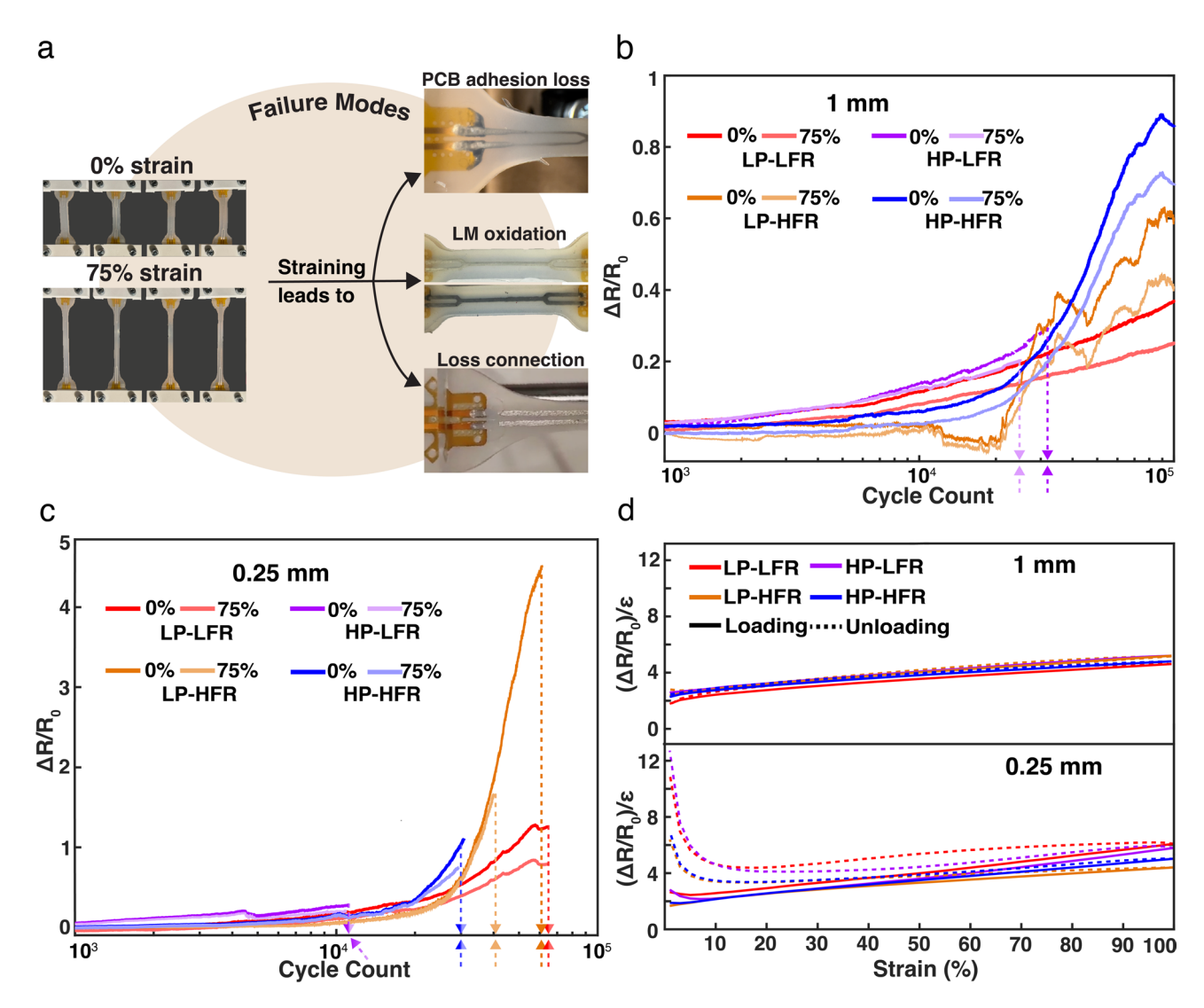


Fig. 4. (a) LMSE failure modes after 100,000 cycles include PCB delamination, LM oxidation, and disconnection at rigid-soft interfaces. (b,c) Resistance increases over cycles due to oxidation, especially in rough, low-flow rate coatings and narrow (0.25 mm) wires, which fail before 100,000 cycles. (d) Gauge factor hysteresis is lower in wider wires with larger cross-sectional areas, influenced by silicone's viscoelasticity and LM flow behavior.

with smooth LM patterns with large cross-sectional area. This can partly be achieved with LP-LFR parameters, but as the flow rate is increased for thicker patterns so is the roughness on soft substrates. Atomization and small particle aerosols are the key principles of spray deposition, so one should look into solutions of enhancing the barrier properties of the encapsulation, as explained before⁵⁸.

Next to long-term reliability, device dynamics are also an important factor in many applications, and LMSE should work precise and consistent over time. Therefore, the hysteresis of the dogbone LMSE in relationship to channel width and various spray parameters is investigated by loading and unloading them up to 100% (to capture a wider array of data points) strain, as shown in Fig. 4d. The gauge factor is plotted over strain, a crucial parameter for determining the suitability of a material as a strain sensor³⁹. Due to the viscoelastic behavior of the polymer and the flow behavior of the LM, considerable hysteresis can occur. The 1 mm wires show very little hysteresis (Fig. S23, Supplementary Information). Hysteresis becomes more severe as the cross-sectional area decreases for 0.25 wide samples. This trend is also true for 0.5 mm and 0.1 mm wide samples (Fig. S24, Supplementary Information). The hysteresis likely arises from LM flow, not encapsulation design (Fig. S25, Supplementary Information). More likely, the hysteresis is due to the LM itself. Upon straining the sample, the LM flows into different areas of the LMSE. Upon releasing the strain, the LM should flow back to its original position as the channel regains its original cross-sectional area. In smaller channels, LM flow is hindered, creating bottlenecks that raise the gauge factor³⁹. Capillary forces are more prevalent, and LM naturally resists these forces due to its high surface tension. Channels narrow most at the strain center, increasing bottlenecks. The oxide layer sticking to channel walls further restricts LM flow. This is also a major issue when LM is deposited via injection⁶¹. Hysteresis is critical, especially in strain-sensing applications, one of the major applications of LMSEs. Low hysteresis is generally preferred, as it reduces the computational load during signal processing. Channels with larger cross-sectional areas should therefore be preferred for strain-sensing applications. This is considered in the following section, where a large strain sensor is presented.

Large-area strain sensor

To demonstrate the large-scale application potential of the process, a 70 by 150 mm large strain sensor with 9 wire loops for human motion sensing is designed and fabricated following the process described in Fig. 1d. The sensor design features straight paths, which are deposited at 65% overlapping paths with a nozzle height of 250 mm (100 mm height would result in non-uniform coatings, which would negatively affect the sensor's printability and reproducibility). The width of the wires is 1 mm, as a large cross-sectional area is most important to ensure a low hysteresis as discussed in the previous section. Pressure must be at a higher value to ensure a reliable yield since printing a large loop-count sensor is prone to misprints. Therefore, the pressure is kept at a value of 4 bar to increase roughness and therefore printability. The flow rate is kept at a lower value of 1 ml/min.

Figure 5a shows the large sensor strained laterally inside a dynamic mechanical analysis (DMA) machine, which is used to extensively study the sensor's electrical and mechanical behavior. Due to the size of the sensor, it is possible to strain it up to 74% in regard to the DMA's limitations, which is sufficient for the targeted human motion sensing applications. At maximum strain at a strain rate of 0.14%/s, the sensor exhibited a resistance

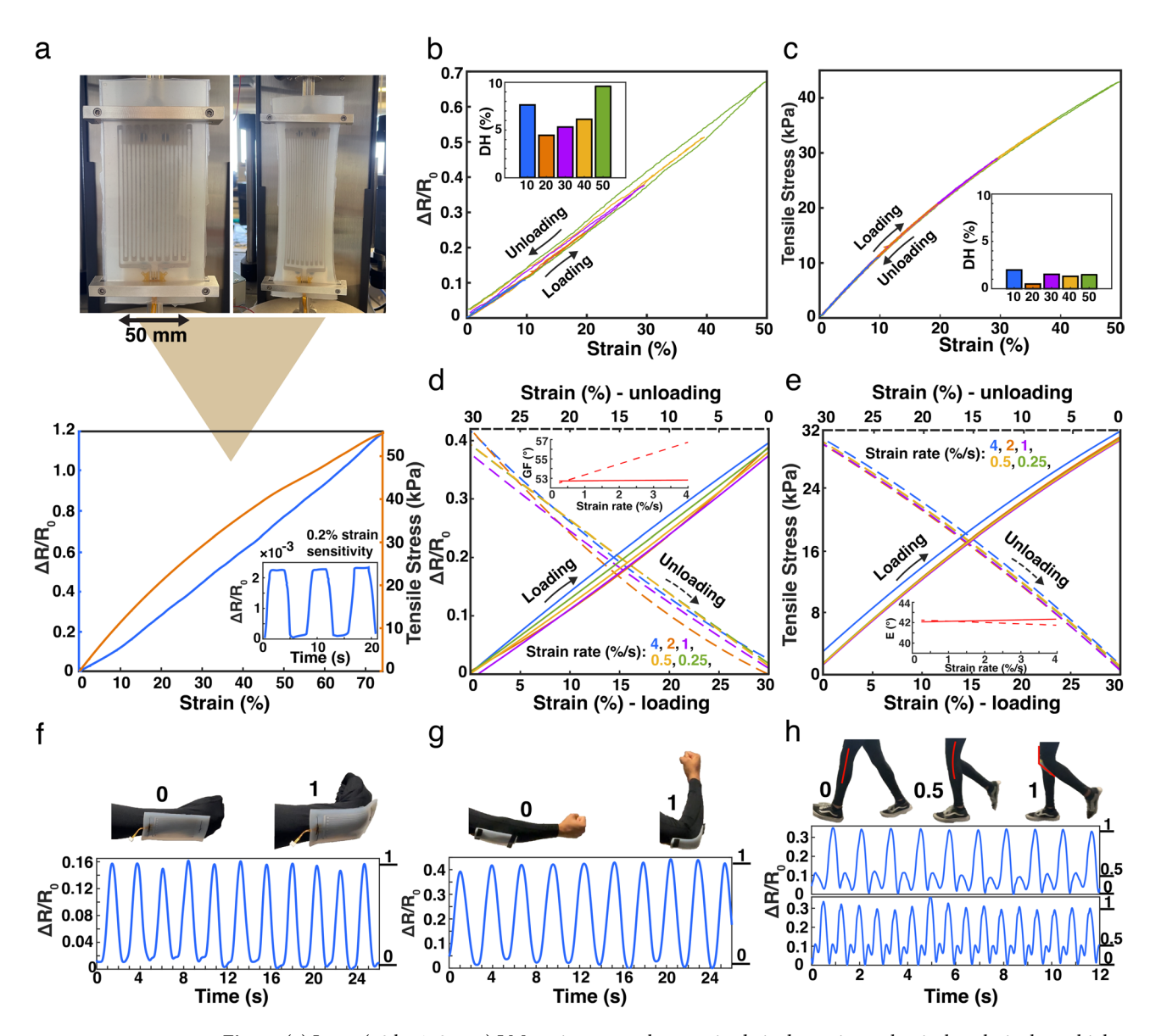


Fig. 5. (a) Large (70 by 150 mm) LM strain sensor characterized via dynamic mechanical analysis shows high sensitivity at 0.2% strain and clear signal response. (b,c) Mullins cycle analysis reveals < 10% hysteresis for $\Delta R/R_0$ at 50% strain and negligible hysteresis for tensile stress, (d,e) Strain rate tests show consistent loading behavior; unloading gauge factor slightly increases at higher rates due to LM flow, (f-h) Real-time motion sensing demonstrates reliable detection of wrist, elbow, and knee movements with distinct resistance peaks.

change of 120%, showing nearly linear behavior. However, at larger strains, the resistance is expected to change quadratically due to the alterations in cross-sectional area and length. As seen in Fig. 5a (insert), the sensors can easily detect strain down to 0.2% (Limit of detection, LOD), which is the bottom noise level of the measurement setup. So far, comparable performance with LMSE has only been achieved with sensors fabricated on a wafer-scale level^{62,63}. This makes the sensor suitable for applications where high sensitivity at a low noise level is needed, such as monitoring physiological parameters⁶⁴.

The sensor is further characterized to evaluate its performance. It underwent a cyclic loading-unloading test, during which it is strained to 10%, 20%, 30%, 40%, and 50% at a constant strain rate of 0.2%/s. The response curves for $\Delta R/R_0$ and stress are presented in Fig. 5b and c, respectively. While there is noticeable hysteresis in the resistance change, this is not as apparent in the stress curve. To quantify the degree of hysteresis, DH(%), the difference between the area under the curves can be calculated using Eq. (3)⁶²:

$$DH(\%) = \left| \frac{A_{loading} - A_{unloading}}{A_{unloading}} \right| \times 100, \tag{3}$$

where A is the area under the loading and unloading curves, respectively. The sensor exhibits a clear trend where the hysteresis increases with maximum strain. A maximum value of <10% at 50% strain is shown in Fig. 5b, a value that is sufficient for accurate data acquisition, as shown further below. This trend and value is expected due to the sensor's multiple lateral loop design and can partly be attributed to the viscoelastic behavior of Ecoflex. During unloading, the channel width may slightly expand compared to the loading phase to maintain a constant volume of liquid metal. This compensates for resilience reduction due to stress relaxation⁶⁵. However, this may not be the sole reason for the hysteresis, as the mechanical hysteresis of the polymer is low, with a maximum value of 1.98% due to its softness, as shown in Fig. 5c. Additionally, the discrepancy in the $\Delta R/R_0$ response between the loading and unloading curves is negative, indicating that $\Delta R/R_0$ is higher during the unloading phase. This suggests that thickness discrepancies and potential bottlenecks may arise due to the flow behavior of the LM. No obvious stress softening is observed in Fig. 5c during the Mullins cycle, suggesting that the Mullins effect is negligible⁶⁶.

The strain rate dependency of the sensor is investigated with strain rates ranging from 0.25%/s to 4%/s for both loading and unloading. The results for $\Delta R/R_0$ and tensile stress are shown in Fig. 5d and e, respectively. Based on the curves alone, the dependencies are not obvious. The slopes in the graphs, for Gauge factor (GF) and Young's modulus (E), calculated using linear regression. The loading curve for GF, as well as both E curves, remains strain-independent, which is generally preferred to minimize processing requirements⁶⁷. However, the GF slightly increases at higher strain rates during unloading, suggesting that the LM does not flow back to its original position as rapidly when unloading occurs at high strain rates.

The sensor is validated in various human motion sensing applications, as shown in Fig. 5f–h. The sensor is woven into the fabric of a bodysuit to prevent displacement during motion. The subject is instructed to perform specific motions, and the $\Delta R/R_0$ sensor response is recorded over time. The values 0, 0.5, and 1 correspond to specific motion states. Figure 5f and g show the sensor being used to monitor wrist and elbow movements, respectively. The curve exhibits distinct and reproducible peaks when the motion concludes. Figure 5h shows the sensor used as a knee sensor to capture leg movement during walking (upper) and running (lower). Walking is characterized by a repetitive sequence known as the gait cycle, which includes noticeable peaks at various stages. In a typical gait pattern, two key peaks are observed: one at 'state 0.5' and another at 'state 1'. The initial phase, 'state 0,' often referred to as 'heel strike,' occurs when the knee angle is nearly straight, close to 0°. The next stage, 'state 1,' or the 'loading response,' shows a brief rise in amplitude followed by a decline in knee angle during the 'mid-stance' phase. At 'state 2,' known as 'toe-off,' the knee angle reaches its maximum point in the cycle. The sensor exhibits consistent peaks corresponding to each stage of the gait cycle. It can also reliably differentiate between distinctive walking and running patterns due to its sensitivity.

The results demonstrate that the sensor, as fabricated by our large-scale process with optimized spray conditions, has great potential to successfully and reliably capture human motion, narrowing the gap between lab-scale and commercially produced LMSE.

Conclusion

This work provides a detailed assessment of how spray parameters affect LMSE properties. This assessment of LMSE fabrication is only feasible with an optimized production process utilizing an in-house automated spray coater that provides full control over pressure, flow rate, height, and pattern. The ASC facilitates a thorough scientific investigation into the scalable LM spraying process due to the system's reproducibility and its compatibility with readily available SMD stencils.

In this study, it is found that both spray parameters and substrate type significantly influence the coating properties. Deposition on hard substrates such as glass results in coatings with lower area roughness at higher pressure. Deposition on soft polymers, which absorb energy, leads to increased roughness at higher pressure or delamination at lower flow rates. Using the ASC, thickness deviations of <5% are achieved with high pressure and flow rate, reducing the risk of bottlenecks. The results also show that spray parameters must be carefully optimized based on the application. For patterns equal to or greater than 0.25 mm, yield is 100% because of the rough patterns ($S_a>5$ μ m, $S_pd>2500$) deposited at high pressure and flow rate (HP-HFR). However, reliability is compromised for rough patterns due to an increase in the rate of $\Delta R/R_0$ over 100,000 stretch cycles. Further, 1 mm wide wires easily withstand 100,000 cycles, while narrow 0.25 mm wide wires fail between 30,000 and 70,000 cycles for strain up to 75%. To demonstrate the advanced scalability of the process, a large, highly sensitive strain sensor is fabricated using the insights gathered from this study and fully characterized.

Category	Suggested combination of pressure and flow rate	Summary of causal relationships
Yield	High flow rate (1.6 mL/min) and high pressure (5 bar) for all stencil widths. Avoid low pressure values (2 bar)	Rough coatings $(S_a>5~\mu m)$ with high peak density $(S_pd>2500)$ are easier to pattern than smooth coatings due to lower cohesion within the bulk
Resolution	High pressure (5 bar) for all pattern widths. Low flow rate (0.7 mL/min) for wide patterns (1 mm), medium flow rate (1.3 mL/min) for narrow patterns (0.5 mm, 0.25 mm)	Rough coatings (S_a > 5 μ m) with high peak density (S_pd > 2500) protect against outwards flow. Thicker patterns with large cross-sectional area are more susceptible to outwards flow
Uniformity	High flow rate (1.6 mL/min) for wider patterns (1 mm, 0.5 mm) and low flow rate (0.7 mL/min) for narrow patterns (0.25 mm). High pressure (5 bar) for all patterns.	Rough coatings $(S_a>5~\mu m)$ with high peak density $(S_pd>2500)$ protect against pushing and lifting liquid metal. High pressure improves atomization. Lower cross-sectional areas are beneficial for narrow patterns
Electrical	High flow rate (1.6 mL/min) and high pressure (5 bar) for all stencil widths.	Spray parameters do not negatively impact electrical properties. Parameters that reliably yield coatings with the largest cross-sectional areas achieve best electrical properties (lowest resistance, $<0.01~\Omega/\mathrm{mm}$)
Reliability	Low flow rate (0.7 mL/min) and low pressure (2 bar) for all stencil widths.	Smooth coatings (S_a > 6 µm, S_pd < 1700) yield up to 4 times lower change resistance over 100,000 cycles than rough coatings due to less oxide buildup
Hysteresis	Low flow rate (0.7 mL/min) for wider patterns (1 mm, 0.5 mm) and high flow rate for narrow patterns (0.25 mm). Low pressure (2 bar) for all stencil widths.	Large cross-sectional area ($>0.04~\mathrm{mm}^2$). Low areas restrict liquid metal flow during stretching due to capillary forces or oxide adhesion. Smoother patterns are better for wide channels

Table 1. Combination of spraying deposition parameters that result in best properties.

The large-area sensor (LOD 0.2%, hysteresis < 10%) reliably captured wrist, elbow, and walking movements. The investigation is comprehensively summarized in Table 1 and identifies which deposition parameters yield the best results for each respective category. This serves as a practical reference for researchers aiming to replicate or tailor LMSE fabrication for specific applications. An outlook for future work to further advance scalability of the process is to automate the stenciling technique.

By thoroughly assessing the spray deposition of LM enabled with the ASC, this work paves the way for scalable production of LMSE, advancing towards reliable devices for soft robotics, consumer electronics, and personal health monitoring.

Methods Materials

Gallium–Indium–Tin (GaInSn) alloy, commonly referred to as "Galinstan," was used as the liquid conductor, with a composition of Ga = 65–95 wt%, In = 5–22 wt%, and Sn = 0–11 wt% (Strategic Elements). Galinstan has a reported melting point between 11°C and -19°C. The silicone elastomer Ecoflex 00-30 (Smooth-On) was employed as the stretchable encapsulation material. It is a soft polymer ideal for LMSE applications, with a 100% modulus of approximately 70 kPa. The custom-designed and patented flex PCBs for reliable interconnections were fabricated from polyamide with ENIG-plated copper pads and were ordered from PCBWay. The 100 μ m thick stainless steel SMD stencils with an aluminum frame were also sourced from PCBWay. The frame stabilizes the stencil during the lifting process.

LMSE fabrication

Fabrication is done in a laboratory with humidity between 36 and 44%, and at constant room temperature. The fabrication process begins with four laser-cut acrylic plates for a single-layer device: a baseplate, an injection plate, and 1st and 2nd cutout plates. First, the flex PCB (and any rigid components) are glued onto the engraved baseplate using a light, water-soluble glue, with the bond pads facing down. The components are then sprayed with silicone adhesion primer (Wacker G790, toluene-free) and left to cure under ambient conditions for 1.5 h. The two-component silicone is mixed in a 50:50 ratio using a speedmixer (Hauschild) and degassed for 20 min. The silicone is then injected into the baseplate–1st cutout–injection plate stack and cured in a 50° C oven for 30 min. Afterward, the substrate is released, flipped, and printed with liquid metal (LM) in the ASC with the stencil, which has a controlled thickness of $100~\mu m$, using varying spray parameters. The optimal range for reproducible devices, as identified in this study, involves a nozzle height of 100-250~mm, a speed of 25~mm/s, a flow rate of 0.7-1.6~ml/min, and a pressure of 2-5~bar. The device is immediately sprayed with primer again, followed by 1.5~h of curing. A slightly wider 2nd cutout is then applied, and processed silicone is blade-coated across the device.

Automated spray coater

The ASC system is based on a customized Tronxy X5SA-Pro 3D printer. The converging spray nozzle was 3D-printed using an SLA printer (Prusa) and attached to the printer's moving bar. The outlet of the nozzle consists of two concentric holes with diameters of 0.75 mm for the LM and 3 mm for the air. The custom motorized syringe, controlled by a stepper motor and Arduino, along with the pressure valve, is operated via the fan control of the 3D printer. Initially, the system was tested with a commercial syringe pump, but irregular flow was observed. The syringe pump and pressure valve are directly connected to the fan control and can be activated using the command "M106 P1 S255", which sets the fan speed to its maximum value and opens the valve.

Spray nozzle characterization

The spray nozzle was characterized separately from the printer, in front of a black background. A green laser in sheet configuration was directed at an angle toward the spray. Images and videos were captured using a Canon EOS 70D camera with an 18–135 mm lens and processed with ImageJ software.

Coating properties

The bulk elemental composition of the coatings was characterized using SEM-EDX (JEOL JSM-IT300). An accelerating voltage of 10 keV was used with a working height of 10 mm. The chemical composition was obtained with EDX. Surface properties were analyzed using a Keyence VK-X250 laser microscope with a 20x objective. Each 3D image was compiled from 80 individual images, with a pitch of 1 μ m. Surface properties were analyzed according to ISO 25178 using Keyence analysis software.

LMSE characterization

The surface properties and dimensions of the LMSE 4-wire devices were characterized using a Keyence VHX-5000 digital microscope, with a pitch of 8 μm across the entire 20 mm length, and analyzed with Keyence software. The bulk resistance of the devices was measured using a Keithley 2400 source meter with 4-wire measurements. Cycle testing was performed using in-house cycle testers capable of testing four devices simultaneously. These testers consist of stepper motors and are controlled by a Python-driven Raspberry Pi. The testers are connected to the source meter and multiplexer, recording temperature and humidity, which are $22.2 \pm 0.42^{\circ} C$ and 49.6 ± 6 %, respectively. Cycle testing was done in a different room than production, which explains the slight differences in humidity. The large strain sensor was mechanically and electrically characterized using a dynamic mechanical analysis (DMA, RSA-G2 TA Instruments) machine, equipped with a Keysight E4980AL LCR meter and custom clamps. For motion sensing applications, the sensor was integrated into a bodysuit and electrically characterized using an Arduino.

Received: 29 June 2025; Accepted: 10 September 2025

Published online: 15 October 2025

References

- 1. Palleau, E., Reece, S., Desai, S. C., Smith, M. E. & Dickey, M. D. Self-healing stretchable wires for reconfigurable circuit wiring and 3d microfluidics. *Adv. Mater.* 25, 1589–1592 (2013).
- 2. Park, Y.-G. et al. Liquid metal-based soft electronics for wearable healthcare. Adv. Healthcare Mater. 10, 2002280 (2021).
- 3. Shintake, J., Cacucciolo, V., Floreano, D. & Shea, H. Soft robotic grippers. Adv. Mater. 30, 1707035 (2018).
- Zhu, S. et al. Ultrastretchable fibers with metallic conductivity using a liquid metal alloy core. Adv. Funct. Mater. 23, 2308–2314 (2013).
- 5. Qi, D., Zhang, K., Tian, G., Jiang, B. & Huang, Y. Stretchable electronics based on pdms substrates. Adv. Mater. 33, 2003155 (2021).
- Wu, W. Stretchable electronics: functional materials, fabrication strategies and applications. Sci. Technol. Adv. Mater. 20, 187–224 (2019).
- 7. Elfferich, J. F., Dodou, D. & Della Santina, C. Soft robotic grippers for crop handling or harvesting: A review. *IEEE Access* 10, 75428–75443 (2022).
- 8. Lin, M., Hu, H., Zhou, S. & Xu, S. Soft wearable devices for deep-tissue sensing. Nat. Rev. Mater. 7, 850-869 (2022).
- 9. Lyu, Q., Gong, S., Yin, J., Dyson, J. M. & Cheng, W. Soft wearable healthcare materials and devices. Adv. Healthcare Mater. 10, 2100577 (2021).
- 10. Guo, R., Wang, X., Yu, W., Tang, J. & Liu, J. A highly conductive and stretchable wearable liquid metal electronic skin for long-term conformable health monitoring. Sci. China Technol. Sci. 61, 1031–1037 (2018).
- 11. Liu, T., Sen, P. & Kim, C.-J. Characterization of nontoxic liquid-metal alloy galinstan for applications in microdevices. *J. Microelectromech. Syst.* 21, 443–450 (2011).
- 12. Foremny, K., Nagels, S., Kreienmeyer, M., Doll, T. & Deferme, W. Biocompatibility testing of liquid metal as an interconnection material for flexible implant technology. *Nanomaterials* 11, 3251 (2021).
- 13. Qin, J. et al. Emerging advances of liquid metal toward flexible sensors. Adv. Mater. Technol. 9, 2300431 (2024).
- 14. Xue, Z. et al. Engineering in-plane silicon nanowire springs for highly stretchable electronics. J. Semicond. 39, 011001 (2018).
- 15. Roels, E. et al. Self-healing sensorized soft robots. Mater. Today Electron. 1, 100003 (2022).
- Kayser, L. V. & Lipomi, D. J. Stretchable conductive polymers and composites based on pedot and pedot: Pss. Adv. Mater. 31, 1806133 (2019).
- 17. Nagels, S. & Deferme, W. Fabrication approaches to interconnect based devices for stretchable electronics: A review. *Materials* 11, 375 (2018).
- 18. Zhu, L., Wang, B., Handschuh-Wang, S. & Zhou, X. Liquid metal-based soft microfluidics. Small 16, 1903841 (2020).
- 19. Tang, S.-Y., Tabor, C., Kalantar-Zadeh, K. & Dickey, M. D. Gallium liquid metal: the devil's elixir. Annu. Rev. Mater. Res. 51, 381–408 (2021).
- 20. Dickey, M. D. Emerging applications of liquid metals featuring surface oxides. ACS Appl. Mater. Interfaces 6, 18369–18379 (2014).
- 21. Wang, B. & Facchetti, A. Mechanically flexible conductors for stretchable and wearable e-skin and e-textile devices. *Adv. Mater.* 31, 1901408 (2019).
- Liu, Y., Pharr, M. & Salvatore, G. A. Lab-on-skin: a review of flexible and stretchable electronics for wearable health monitoring. ACS Nano 11, 9614–9635 (2017).
- 23. Li, G. et al. High-efficiency large-area printed multilayer liquid metal wires for stretchable biomedical sensors with recyclability. ACS Appl. Mater. Interfaces 13, 56961–56971 (2021).
- 24. Ma, J. et al. Shaping a soft future: patterning liquid metals. Adv. Mater. 35, 2205196 (2023).
- 25. Neumann, T. V. & Dickey, M. D. Liquid metal direct write and 3d printing: a review. Adv. Mater. Technol. 5, 2000070 (2020).
- 26. Yoon, Y., Kim, S., Kim, D., Kauh, S. K. & Lee, J. Four degrees-of-freedom direct writing of liquid metal patterns on uneven surfaces. *Adv. Mater. Technol.* 4, 1800379 (2019).
- 27. Chen, H.-Y. & Conn, A. T. A stretchable inductor with integrated strain sensing and wireless signal transfer. *IEEE Sens. J.* 20, 7384–7391 (2020).
- 28. Lin, Y. et al. Vacuum filling of complex microchannels with liquid metal. Lab Chip 17, 3043-3050 (2017).
- 29. Kim, J.-H. et al. Imbibition-induced selective wetting of liquid metal. Nat. Commun. 13, 4763 (2022).
- 30. Jiang, Y. et al. Selective wetting/dewetting for controllable patterning of liquid metal electrodes for all-printed device application. *J. Mater. Chem. C* 5, 12378–12383 (2017).
- 31. Lazarus, N., Bedair, S. S. & Kierzewski, I. M. Ultrafine pitch stencil printing of liquid metal alloys. ACS Appl. Mater. Interfaces 9, 1178–1182 (2017).
- 32. Wang, L. & Liu, J. Pressured liquid metal screen printing for rapid manufacture of high resolution electronic patterns. RSC Adv. 5, 57686–57691 (2015).
- 33. Zhang, Q., Gao, Y. & Liu, J. Atomized spraying of liquid metal droplets on desired substrate surfaces as a generalized way for ubiquitous printed electronics. *Appl. Phys. A* **116**, 1091–1097 (2014).

- Neumann, T. V. et al. Aerosol spray deposition of liquid metal and elastomer coatings for rapid processing of stretchable electronics. *Micromachines* 12, 146 (2021).
- 35. Jeong, S. H., Hjort, K. & Wu, Z. Tape transfer atomization patterning of liquid alloys for microfluidic stretchable wireless power transfer. Sci. Rep. 5, 8419 (2015).
- 36. Elassy, K. S., Akau, T. K., Shiroma, W. A., Seo, S. & Ohta, A. T. Low-cost rapid fabrication of conformal liquid-metal patterns. *Appl. Sci.* 9, 1565 (2019).
- 37. Melcher, J. L. et al. Spray-on liquid-metal electrodes for graphene field-effect transistors. Micromachines 10, 54 (2019).
- 38. Fangohr, H., Chernyshenko, D. S., Franchin, M., Fischbacher, T. & Meier, G. Joule heating in nanowires. *Phys. Rev. B Condensed Matter Mater. Phys.* 84, 054437 (2011).
- 39. Yao, B. et al. Ultrasensitive, highly stable, and stretchable strain sensor using gated liquid metal channel. *Adv. Funct. Mater.* 1, 2314298 (2024).
- 40. Frey, E. J., Im, S., Bachmann, A. L., Genzer, J. & Dickey, M. D. Patterning of a high surface area liquid metal-carbon composite film using laser processing. *Adv. Funct. Mater.* 34, 2308574 (2024).
- 41. Khan, M. A., Gadgil, H. & Kumar, S. Influence of liquid properties on atomization characteristics of flow-blurring injector at ultralow flow rates. *Energy* 171, 1–13 (2019).
- 42. Cook, A. et al. Shear-driven direct-write printing of room-temperature gallium-based liquid metal alloys. Adv. Eng. Mater. 21, 1900400 (2019).
- 43. Jung, W. et al. Solvent-assisted filling of liquid metal and its selective dewetting for the multilayered 3d interconnect in stretchable electronics. ACS Nano 16, 21471–21481 (2022).
- 44. Dickey, M. D. et al. Eutectic gallium-indium (egain): a liquid metal alloy for the formation of stable structures in microchannels at room temperature. *Adv. Funct. Mater.* **18**, 1097–1104 (2008).
- 45. Song, M. et al. Overcoming Rayleigh-plateau instabilities: Stabilizing and destabilizing liquid-metal streams via electrochemical oxidation. *Proc. Natl. Acad. Sci.* 117, 19026–19032 (2020).
- 46. Freddi, A., Salmon, M., Freddi, A. & Salmon, M. Introduction to the taguchi method. Design Principles and Methodologies: From Conceptualization to First Prototyping with Examples and Case Studies 159–180 (2019).
- 47. Balsari, P., Grella, M., Marucco, P., Matta, F. & Miranda-Fuentes, A. Assessing the influence of air speed and liquid flow rate on the droplet size and homogeneity in pneumatic spraying. *Pest Manag. Sci.* 75, 366–379 (2019).
- 48. Nasr, G. G. et al. Studies of high pressure water sprays from full cone atomizers. ILASS-Europe, Toulouse, France 1-6 (1999).
- 49. Steven Nagels, W. D. & Vandenryt, T. Interconnect, an Electronic Assembly and a Method for Manufacturing an Electronic Assembly (2019)
- 50. Wu, Q. et al. Suspension printing of liquid metal in yield-stress fluid for resilient 3d constructs with electromagnetic functions. NPJ Flexible Electron. 6, 50 (2022).
- 51. ISO-Organization. Plastics—Determination of Tensile Properties, Part 1 (2019).
- 52. Arola, D. & Williams, C. Estimating the fatigue stress concentration factor of machined surfaces. Int. I. Fatigue 24, 923–930 (2002).
- 53. Wang, X. et al. Liquid metal bionic instant self-healing flexible electronics with full recyclability and high reliability. *Chem. Eng. J.* 431, 133965 (2022).
- 54. Handschuh-Wang, S. et al. The subtle difference between galinstan (r) and eutectic gainsn. Materialia 26, 101642 (2022).
- 55. Xu, C., Ma, B., Yuan, S., Zhao, C. & Liu, H. High-resolution patterning of liquid metal on hydrogel for flexible, stretchable, and self-healing electronics. *Adv. Electron. Mater.* **6**, 1900721 (2020).
- 56. Feng, B. et al. Nacre-inspired, liquid metal-based ultrasensitive electronic skin by spatially regulated cracking strategy. *Adv. Funct. Mater.* **31**, 2102359 (2021).
- Oh, J. et al. A liquid metal based multimodal sensor and haptic feedback device for thermal and tactile sensation generation in virtual reality. Adv. Funct. Mater. 31, 2007772 (2021).
- Sahraeeazartamar, F. et al. Diels-alder network blends as self-healing encapsulants for liquid metal-based stretchable electronics. ACS Appl. Mater. Interfaces 16, 34192–34212 (2024).
- 59. Sanchez-Botero, L., Shah, D. S. & Kramer-Bottiglio, R. Are liquid metals bulk conductors? Adv. Mater. 34, 2109427 (2022).
- IPC-International. IPC-9701—Revision A—Performance Test Methods and Qualification Requirements for Surface Mount Solder Attachments (2006).
- 61. Kramer, R. K., Boley, J. W., Stone, H. A., Weaver, J. C. & Wood, R. J. Effect of microtextured surface topography on the wetting behavior of eutectic gallium–indium alloys. *Langmuir* 30, 533–539 (2014).
- 62. Luo, Y. et al. Flexible liquid metal-based microfluidic strain sensors with fractal-designed microchannels for monitoring human motion and physiological signals. *Biosens. Bioelectron.* **246**, 115905 (2024).
- 63. Wu, Y. et al. Liquid metal-based strain sensor with ultralow detection limit for human–machine interface applications. *Adv. Intell. Syst.* 3, 2000235 (2021).
- 64. Dinh, T. et al. Stretchable respiration sensors: Advanced designs and multifunctional platforms for wearable physiological monitoring. *Biosens. Bioelectron.* 166, 112460 (2020).
- 65. Chen, J. et al. Superelastic, sensitive, and low hysteresis flexible strain sensor based on wave-patterned liquid metal for human activity monitoring. ACS Appl. Mater. Interfaces 12, 22200–22211 (2020).
- 66. Zhang, S., Ge, C. & Liu, R. Mechanical characterization of the stress-strain behavior of the polydimethylsiloxane (pdms) substate of wearable strain sensors under uniaxial loading conditions. Sens. Actuators A 341, 113580 (2022).
- 67. Nankali, M. et al. Highly stretchable and sensitive strain sensors based on carbon nanotube-elastomer nanocomposites: the effect of environmental factors on strain sensing performance. *J. Mater. Chem. C* 8, 6185–6195 (2020).

Author contributions

M.K.: Conceptualization, investigation, data curation, methodology, formal analysis and draft writing; R.N.S.: Investigation (Fig. 5 sensor design and characterisation); L.P.: Investigation (Fig. 4 cycle testing); P.V.S.: Investigation (Fig. 2 SEM/EDX); D.R.: Investigation (Fig. 1 spray visualisation); F.S.: Investigation (Fig. 4 Dogbone tensile test); J.B.: Supervision; G.V.A.: Supervision; I.D.G.: Supervision; T.H.: Supervision; M.D.: Supervision; S.T.: Supervision; B.V.: Supervision; M.R.: Supervision, formal analysis and review and editing of the original draft; W.D.: Supervision, review and editing, funding acquisition, project administration.

Funding

Funding is provided for Maximilian Krack by the Fonds Wetenschappelijk Onderzoek (FWO, 1SH1C24N) and the Bijzonder Onderzoeksfonds (BOF, BOF23INCENT17). FWO is additionally providing funding within the broader SBO project of SUBLIME (S007423N).

Declarations

Competing interests

The authors declare no competing interests.

Additional information

Supplementary Information The online version contains supplementary material available at https://doi.org/1 0.1038/s41598-025-19775-0.

Correspondence and requests for materials should be addressed to W.D.

Reprints and permissions information is available at www.nature.com/reprints.

Publisher's note Springer Nature remains neutral with regard to jurisdictional claims in published maps and institutional affiliations.

Open Access This article is licensed under a Creative Commons Attribution-NonCommercial-NoDerivatives 4.0 International License, which permits any non-commercial use, sharing, distribution and reproduction in any medium or format, as long as you give appropriate credit to the original author(s) and the source, provide a link to the Creative Commons licence, and indicate if you modified the licensed material. You do not have permission under this licence to share adapted material derived from this article or parts of it. The images or other third party material in this article are included in the article's Creative Commons licence, unless indicated otherwise in a credit line to the material. If material is not included in the article's Creative Commons licence and your intended use is not permitted by statutory regulation or exceeds the permitted use, you will need to obtain permission directly from the copyright holder. To view a copy of this licence, visit https://creativecommons.org/licenses/by-nc-nd/4.0/.

© The Author(s) 2025